Quantum Confinement Controls Photocatalysis: A Free Energy Analysis for Photocatalytic Proton Reduction at CdSe Nanocrystals

Jing Zhao, Michael A. Holmes, and Frank E. Osterloh*

Department of Chemistry, University of California, Davis, One Shields Avenue, Davis, California 95616, United States

ABSTRACT The ability to adjust the mechanical, optical, magnetic, electric, and chemical properties of materials *via* the quantum confinement effect is well-understood. Here, we provide the first quantitative analysis of quantum-size-controlled photocatalytic H_2 evolution at the semiconductor–solution interface. Specifically, it is found that the hydrogen evolution rate from illuminated suspended CdSe quantum dots in aqueous sodium sulfite solution depends on nanocrystal size. Photoelectrochemical measurements on CdSe nanocrystal films reveal that the observed reactivity is controlled by the free energy change of the system, as determined by the proton reduction potential and the quasi-Fermi energy of the dots. The corresponding free energy change can be fitted to the photocatalytic activity using a modified Butler–Volmer equation for reaction kinetics. These findings establish a quantitative experimental basis for quantum-confinement-controlled proton reduction with semiconductor nanocrystals. Electrochemical data further indicate that proton reduction occurs at cadmium sites on the dots, and that charge separation in these nanocrystals is controlled by surface effects, not by space charge layers.

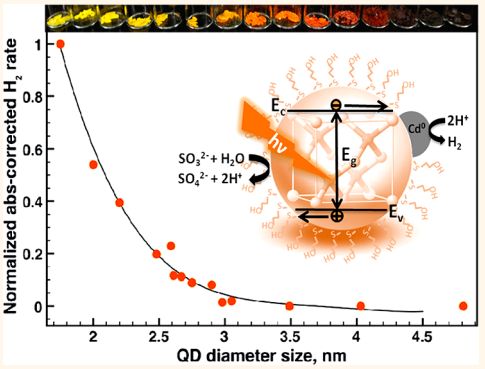

KEYWORDS: quantum confinement · quantum dot · photolysis · water splitting · solar fuel · Butler–Volmer · space charge layer

Semiconductor and metal nanocrystals with sizes below the Bohr exciton radius exhibit quantum confinement effects, which modify the optical,[1−4] electrical,[5] magnetic,[6,7] and chemical[8,9] properties of materials. These tunable properties make semiconductor nanocrystals especially interesting for solar energy conversion applications and as photocatalysts.[10−22] According to Marcus theory, quantum-confined systems support higher rates of interfacial charge transfer, due to the increased thermodynamic energy of the confined electron–hole pairs.[23,24] For *solid–solid* interfaces, quantum-controlled electron injection has been experimentally confirmed for CdTe/CdSe core–shell and nanorod structures[25,26] and for CdSe and PbS dots immobilized on TiO_2.[27−30] As Kamat's group showed recently,[27−32] the dependence of the interfacial charge transfer rates on the energetics of these systems can be quantitatively understood using Marcus theory. For *solid–liquid* interfaces, a comparable theoretical analysis is still lacking, even though quantum-confinement-controlled redox reactions have been observed for a number of systems. For electron transfer between CdSe dots (2.3–6.3 nm in diameter) and methylviologen cations, Wachtveitl and co-workers noted an exponential dependence of the electron transfer rate on the free energy change.[33] For CdSe dots with adsorbed Re-bipyridyl complexes,[34] or covalently linked fullerene derivatives,[31] photochemical electron transfer rates were found to increase with decreasing size of the dots. Several instances of a quantum effect in photocatalytic reactions were also reported but only qualitatively. For example, WO_3 nanocrystal suspensions showed a size dependence for the decomposition of benzene[35] and for photocatalytic water oxidation.[36] Cadmium sulfide nanoparticles were reported to exhibit a size-dependent activity for

* Address correspondence to fosterloh@ucdavis.edu.

Received for review February 18, 2013 and accepted April 16, 2013.

Published online April 16, 2013
10.1021/nn400826h

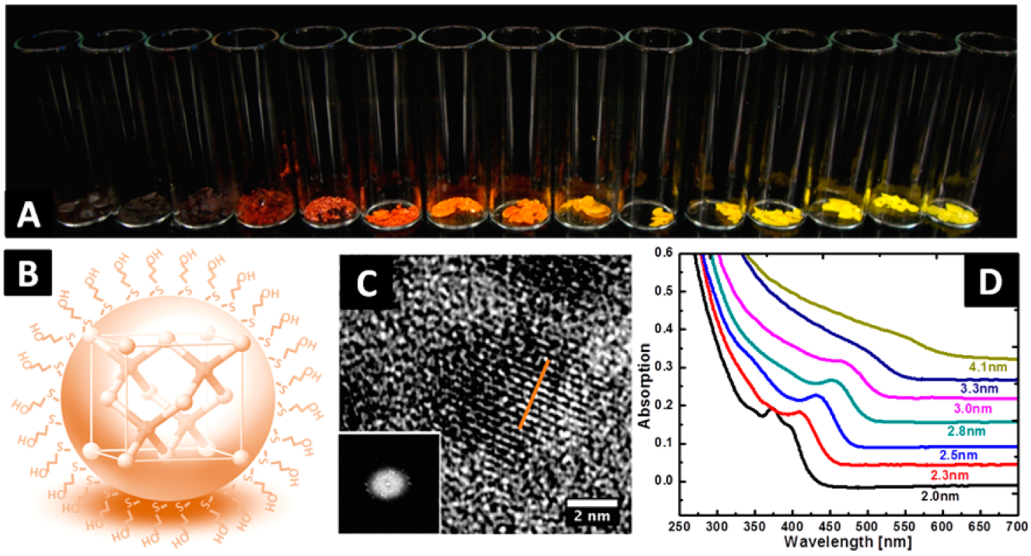

Figure 1. (A) Photos of CdSe QD powders (first left, bulk CdSe; second left to right and so on, CdSe QDs with sizes from 6.0 to 2.1 nm). (B) Schematic diagram of CdSe QD structure with a zinc blende crystal phase and 2-mercaptoethanol surface ligands. (C) HR-TEM image of a 4.8 nm QD as viewed along the [011] ozone axis with an inset showing the electron diffraction patterns from (111) and (022) Bragg planes of the cubic structure type. (D) UV−vis absorption spectra of QD solutions with various sizes.

photoreduction of aromatic ketones[37] and for methanol dehydrogenation.[38] Cadmium selenide nanoribbons with a 2.7 eV expanded band gap were found to photocatalytically produce hydrogen from irradiated Na_2SO_3/NaSH solution, whereas bulk CdSe (E_g = 1.7 eV) was not active.[39,40] We recently reported that the hydrogen evolution rates from illuminated CdSe quantum dot (QD) suspensions in Na_2SO_3 solution showed a logarithmic dependence on the semiconductor band gap.[41] We have now been able to measure the precise energetics of the dots with electrochemical techniques and perform a thorough analysis of the observed reactivity trend. The results show that the kinetics of hydrogen evolution in this system can be understood quantitatively using a modified Butler−Volmer model, which relates the kinetic activation energy with the thermodynamic free energy change for proton reduction. These findings establish an experimental basis for quantum-confinement-controlled photocatalytic hydrogen evolution with nanocrystals. The data further show that proton reduction proceeds on the cadmium sites on the CdSe QD surface, and that charge transport in CdSe QDs occurs by diffusion, not by drift, as postulated by Kronik,[42] Gratzel,[43] Hagfeld,[44] and Memming.[45] These results have an impact on the use of quantum-size-confined semiconductors for solar energy conversion[46] and on the understanding of reaction kinetics in nanostructured photocatalysts and photoelectrodes.[17,47]

RESULTS AND DISCUSSION

Monodisperse CdSe quantum dots with a diameter ranging from 1.8 to 6.0 nm were synthesized using 2-mercaptoethanol as a short-chain surface-passivating agent (Figure 1A,B) based on a known procedure by Rogach *et al.*,[48] followed by size-selective precipitation with 2-propanol. According to HR-TEM (Figure 1C) and powder XRD (Supporting Information Figure S1) data, these QDs are single crystals of the cubic zinc blende structure type. The preference of the zinc blende over the wurtzite structure type is well-known for CdSe quantum dots.[41,48] Optical properties of the QD powders (Figure 1A) are size-dependent, which is a direct outcome of the increase in their band gaps. Optical band gaps for these QDs range from 2.04 to 2.90 eV (absorption onsets between 607 and 427 nm) for sizes between 4.1 and 2.0 nm according to their UV−vis absorption spectra (Figure 1D), while bulk CdSe has a band gap of 1.76 eV (704 nm). This widening of the optical band gap as size decreases into the quantum confinement regime has been modeled and observed for many materials[1,49−52] and is consistent with many previous studies on CdSe QDs.[48,53,54]

To determine the photocatalytic activity of these dots, particle suspensions were irradiated with light (>330 nm, 400 mW/cm^2) in the presence of 0.10 M aqueous Na_2SO_3 as a sacrificial agent. Sodium sulfite was selected instead of sodium hydrosulfide because the latter was found to induce precipitation of the CdSe QDs *via* cross-linking. Sulfite is less active than sulfide but does protect CdSe against photocorrosion[39,40,55,56] by reacting with the photogenerated holes, as shown in the inset of Figure 2B. We have previously reported that, under these conditions, all QD samples, except for the largest particles and bulk CdSe, evolved hydrogen linearly over time (Figure 2A).[41] Interestingly, a lag occurs between the beginning of illumination and the beginning of H_2 evolution. This lag ranges between

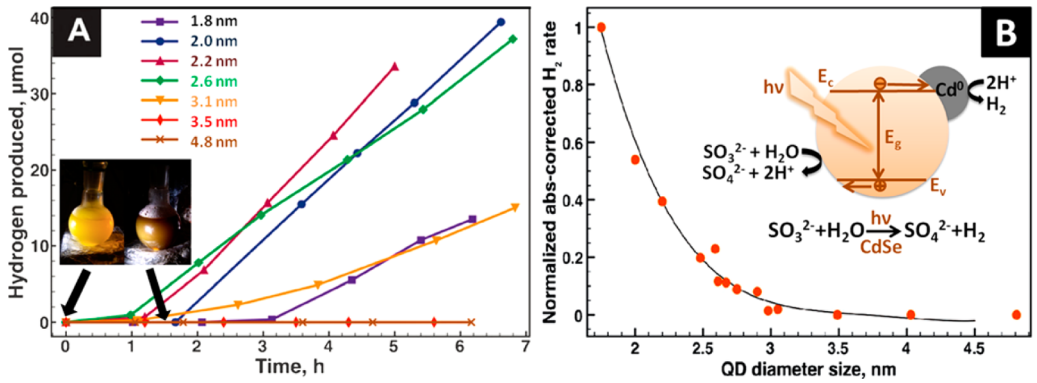

Figure 2. (A) Experimental H_2 evolution from CdSe QDs in 0.10 M Na_2SO_3 aqueous solution at pH 9.2. Inset: Photos showing visible color change of CdSe QD solution before (left) and during (right) irradiation. (B) Relative H_2 evolution rates as normalized with regard to catalyst amount and absorbed photons plotted *vs* QD size. Inset: Schematic diagram of hydrogen evolution at CdSe QDs in the presence of sodium sulfite.

0.5 and 3 h and roughly increases with inverse particle size. It is accompanied by the formation of a brown color (inset of Figure 2A), which disappears upon exposing the dots to air. This suggests that the color change corresponds to the *in situ* formation of Cd^0 on the dot surface, which might be necessary for the catalytic hydrogen evolution. The longer lag times for the smaller CdSe dots could be interpreted as a result of the greater cadmium nucleation barrier. Attempts to directly observe the formed cadmium particles with electron microscopy failed due to the small size and the air sensitivity of the formed cadmium. We note, however, that the formation of metal particles during photocatalysis has previously been reported for ZnS photocatalysts.[56] Correcting the H_2 evolution rates in Figure 2A for catalyst mass and absorbed photons (for details see Supporting Information Figure S2) and plotting them *versus* size gives the trend in Figure 2B. A monotonic increase in hydrogen evolution rate with decreasing particle size is evident. This suggests that hydrogen evolution activity of these QDs is regulated by the energetics of the charge carriers in the particles.

In order to quantitatively understand the relationship between QD size, QD energetics, and their photocatalytic activity, the energetics of the QDs were studied in detail with electrochemistry and photoelectrochemistry. Electrodes of quantum dot films (1.0 × 1.0 cm^2) were prepared by drop-coating QD solutions on F/SnO_2 substrates and drying in the dark overnight. The films were immersed in an aqueous electrolyte containing 1.0 M KCl and 0.10 M Na_2SO_3 at a pH of 9.2 in all of the measurements. Sulfite was used as the sacrificial donor over sulfide because, as a potential determining ion, sulfide can fix the Fermi level of CdSe.[40,57] The use of sulfite also ensured compatibility with the photocatalytic hydrogen evolution experiments. Photocurrent scans were performed cathodically from 0.4 to −1.7 V *vs* NHE under illumination with chopped light from a xenon arc lamp. The results are shown in Figure 3 for various sizes.

In general, photocurrents were small for bulk CdSe (60 $\mu A/cm^2$) and for small QDs below 2.6 nm (10 $\mu A/cm^2$) but larger for large QDs above 2.6 nm (300 $\mu A/cm^2$). This trend can be explained by several competing factors, which includes an increase in surface area in going from bulk CdSe to large QDs and a decrease of the photon absorption in going from large to smaller QDs. Besides, the non-annealed QD films also have a large electrical resistance since electron transport has to occur by thermally activated hopping and/or electron tunneling between dots.[44,58−63] Smaller QDs lead to more junctions between the dots, thus a higher resistance is expected.

The most interesting aspect of the scans is that QDs with diameters above 2.6 nm produced large anodic photocurrents, whereas QDs with diameters below 2.6 nm produced small cathodic photocurrents, as shown in Figure 3A,B. For large dots (>2.6 nm), the size of the anodic current was a strong function of the applied potential and occurred only positive of an onset potential E_{Ph} that was characteristic for each CdSe film (Figure 3A). For instance, E_{Ph} varies from −0.51 V for bulk CdSe to −0.75 V for 4.0 nm dots and −1.13 V for 2.8 nm dots. On the contrary, small QDs (<2.6 nm) produced only a small (10 $\mu A/cm^2$) cathodic photocurrent, whose magnitude was nearly independent of the applied potential or QD diameter (Figure 3B). Interestingly, all of the cathodic photocurrents showed a similar photo-onset E_{Ph} near −0.3 V. In addition, a small anodic photocurrent at potentials positive of −0.1 V was observed, but this signal originated from the F/SnO_2 electrode background, not from the QD film (see bottom trace in Figure 3B). The observed photocurrent inversion in going from large to small CdSe QDs is not unprecedented in the literature. It has been previously observed by Kronik and coworkers for CdSe dot films from before to after hydrochloric acid etching and been assigned to the charge trapping at surface sites.[64−66] Our results and the following discussion support this interpretation.

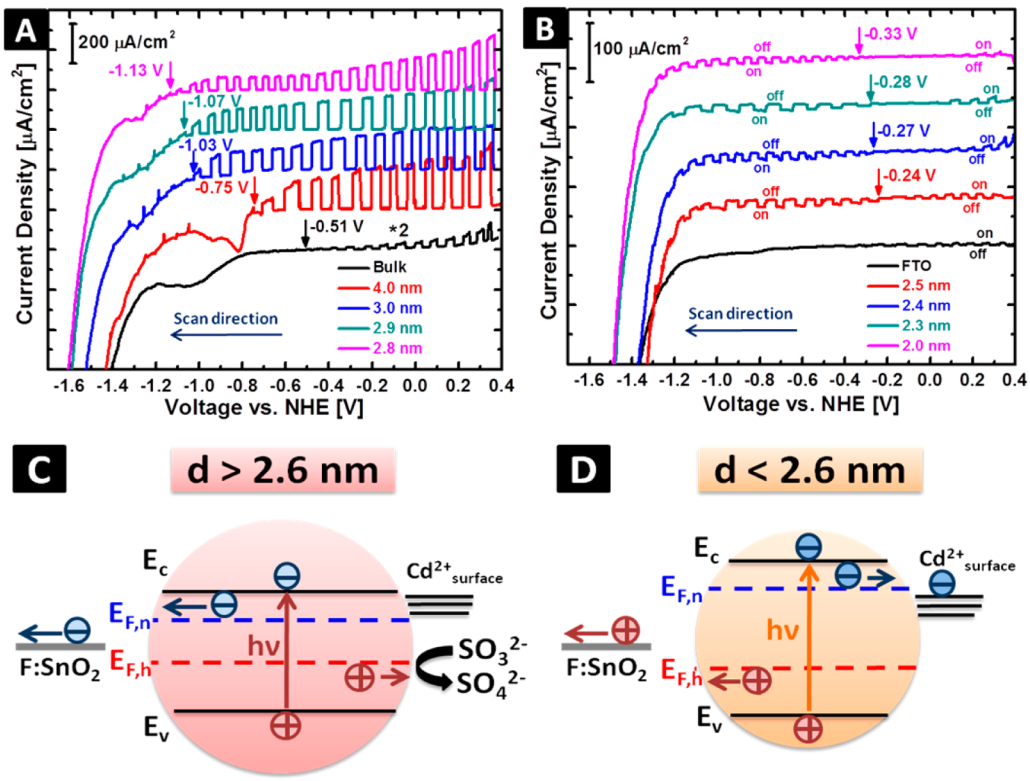

Figure 3. (A,B) Photoelectrochemical scans of CdSe QD films on F/SnO_2 electrodes with a scan rate of 10 mV/s at pH 9.2 in 1.0 M KCl/0.10 M Na_2SO_3 aqueous solutions for various sizes under investigation. Large QDs above 2.6 nm show anodic photocurrents with onsets indicated by the arrows in (A), whereas small QDs below 2.6 nm establish cathodic photocurrents with onsets near −0.3 V, as indicated by the arrows in (B). Note that photocurrent for bulk CdSe in (A) is enlarged for better visibility. (C,D) Schematic diagrams demonstrating the anodic to cathodic photocurrent switch when going from large to small QDs. Surface Cd^{2+} states are present in these CdSe QDs, which could undergo photochemical or electrochemical reduction and lead to Cd^0 *in situ* formation on QD surface. For large QDs (>2.6 nm) with $E_{F,n}$ below surface Cd^{2+} sites, photoelectrons can be extracted by F/SnO_2 electrode at its $E_{F,n}$ level, resulting in an anodic photocurrent. For small QDs (<2.6 nm), $E_{F,n}$ is above surface Cd^{2+} sites due to quantum confinement shift; therefore, photoelectrons get preferentially trapped at surface sites. Instead, photoholes are extracted by F/SnO_2 electrode at its $E_{F,h}$, leading to a cathodic photocurrent.

As an n-type material, bulk CdSe normally forms a depletion layer when in contact with a suitable redox couple in the liquid phase (*e.g.*, H^+/H_2). However, the QDs investigated here are too small to allow a full space charge layer to develop. Assuming a donor concentration of $n_D = 1.5 \times 10^{17}$ cm^{-3},[67] a dielectric constant of $\varepsilon_r = 9$ for CdSe, and a full depletion case, the space charge layer is 80 nm wide[68]—20 times larger than the diameter of the dots. Under these conditions, the potential barrier within the dots is limited by the nanocrystal diameter and does not exceed 3.9 meV for a 2.0 nm dot or 17 meV for a 4.2 nm dot, as calculated using the method by Albery.[69,70] Such a barrier is not effective for electrons at room temperature (thermal energy $kT = 26$ meV), which means that, instead of surface band bending, other factors determine the charge separation at the QD−liquid interface. We attribute the observed inversion of the photocurrent to the preferential trapping of electrons at Cd^{2+} surface states, as shown in Figure 3C,D. For the large QDs (>2.6 nm), these Cd^{2+} surface states are not accessible because their energy is above the quasi-Fermi energy of the photogenerated electrons $E_{F,n}$. As a result, an anodic photocurrent is observed due to the sulfite oxidation by photogenerated holes and the extraction of photoelectrons at the back electrode when the applied potential is positive of $E_{F,n}$. Thus, the photo-onset E_{Ph} is a measure of the Fermi energy of the electrons $E_{F,n}$ in the dots. In the small QDs (<2.6 nm), on the other hand, the Fermi energy of the electrons $E_{F,n}$ has been raised due to quantum confinement effect. Consequently, these photogenerated electrons become preferentially trapped at surface Cd^{2+} ions to produce Cd^0. A cathodic photocurrent is observed, due to the extraction of photogenerated holes by the back electrode when the applied potential at the electrode is negative of the quasi-Fermi level for holes $E_{F,h}$. Due to the low mobility of the holes, the cathodic photocurrents in the small dots are much lower than the anodic photocurrents in the large dots. Importantly, the onset potential for the cathodic current in the small dots is no longer a good measure of the quasi-Fermi level for electrons $E_{F,n}$. As it turns out, $E_{F,n}$ can be estimated from electrochemical scans in the dark instead. Three reduction features can be discerned in the dark scans, which are labeled as I, II, and III (Figure 4).

Features I and II are associated with each other and shift cathodically from −0.73 and −1.05 V for dots of 4.2 nm, to −1.06 and −1.35 V for dots of 3.0 nm, and −1.14 and −1.37 V for dots of 2.8 nm (Figure 4, Table 1, and Figure S3). These reduction peaks do not lead to any visible gas evolution but induce a visible brown coloration of the films. The same color was also observed during irradiation of the dots in the presence of Na_2SO_3 (Figure 2A inset). Thus, reduction peaks I and II are attributed to the reduction of surface and lattice Cd^{2+} ions, respectively. The observed reduction peak potentials compare well to literature values.

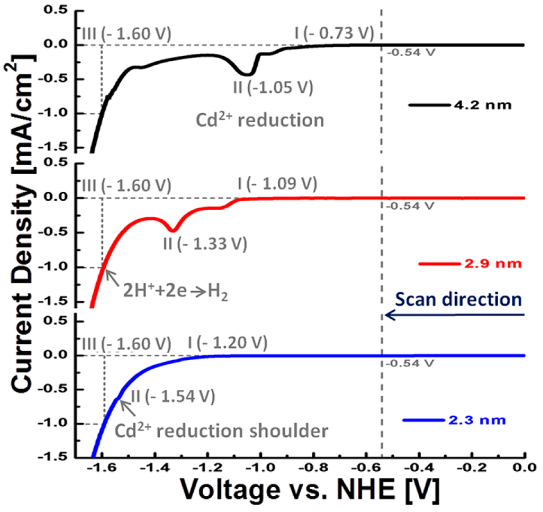

Figure 4. Selected dark electrochemical scans of CdSe QD films on F/SnO_2 electrodes with a scan rate of 10 mV/s at pH 9.2 in 1.0 M KCl/0.10 M Na_2SO_3 aqueous solutions for three representative diameters. Additional scans for all other sizes are available in the Supporting Information (Figure S3). The vertical gray dashed line at −0.54 V *vs* NHE indicates the Nernst potential for proton reduction to hydrogen at pH 9.2. Electrochemical proton reduction potentials (feature III) are determined at a current density of 1.0 mA/cm^2, as indicated by the gray dotted lines. Features I (onset) and II (maximum) are assigned to the reduction of surface and lattice Cd^{2+} sites, respectively.

For example, 6.5 nm TOPO-coated CdSe dots undergo Cd^{2+} reduction at −1.06 V *vs* NHE in acetonitrile,[71] and for 2.8 nm thioglycolic acid-capped CdTe dots, Cd^{2+} reduction is observed at −1.40 V *vs* NHE.[72] Adding electrons to lattice Cd^{2+} sites is equivalent to adding electrons to the CdSe conduction band; therefore, the reduction peak potential is a good indication of E_{CB} in the CdSe dots and is listed in Table 1, together with other parameters. Indeed, for QDs with diameters larger than 2.6 nm, Cd^{2+} reduction features in Figures 4 and S3 occurred slightly negative of the photo-onset potentials $E_{ph} = E_{F,n}$ in Figure 3A. For example, in 4.2 nm dots, E_{Ph} = −0.72 V and $E(Cd^{2+}/Cd)$ = −1.05 V, and for 2.9 nm dots, E_{Ph} = −1.07 V and $E(Cd^{2+}/Cd)$ = −1.33 V. The observed $E_{CB}-E_{F,n}$ separation of 0.25−0.30 V indicates that the QDs are weakly n-doped. For QDs with diameters below 2.6 nm, the Cd^{2+} reduction peak shifts further cathodically and merges with feature III near −1.6 V, only observable as a shoulder (Figures 4 and S3). Therefore, for the smallest dots (<2.6 nm), E_{CB} is determined from the shoulder potential. As $E_{F,n}$ in these dots cannot be obtained from the cathodic photocurrent onsets, $E_{F,n}$ values are estimated using the measured E_{CB} to be negative of −1.13 V ($E_{F,n}$ of the closest 2.8 nm QD) and at least 0.059 V positive of the corresponding E_{CB} (Table 1).

Cathodic feature III in the dark scan (Figure 4) occurs near −1.6 V. This feature is associated with the reduction of protons, as evident from the observed H_2 gas evolution at the electrode. A Tafel plot in Figure S4 presents the linear regime of the logarithmic current density log(|*i*|) *versus* the applied potential curves for proton reduction over various QD films.

$$\log(|i|) = -\frac{\alpha F}{2.303RT}E + \log(|i_0|) \qquad (1)$$

As indicated by eq 1 for the Tafel plot, extrapolating the linear fit to zero applied potential yields the exchange current density i_0 from the intercept. Values for the different QD films fall into a narrow interval between

TABLE 1. Summary of Energetic Properties for CdSe QDs[a]

diameter/nm	E_g /eV	E_{ph}[b]/V	$E_{F,n}$[c]/V	$E_{F,h}$[d]/V	E_{CB}[e]/V	E_{VB}[f]/V	$E(Cd^{2+}/Cd)_{surface}$[g]/V	normalized H_2 evolution rate[i]
bulk	1.74	−0.51	−0.51	NA	−0.85	0.89	−0.67	NA
4.2	1.97	−0.72	−0.72	NA	−1.05	0.92	−0.73	<0.001
4.0	2.05	−0.75	−0.75	NA	−1.05	1.00	−0.75	0.002
3.0	2.39	−1.03	−1.03	NA	−1.35	1.04	−1.06	0.050
2.9	2.43	−1.07	−1.07	NA	−1.33	1.10	−1.09	0.070
2.8	2.47	−1.13	−1.13	NA	−1.37	1.10	−1.14	0.085
2.5	2.58	−0.24	−1.13...−1.31[h] (−1.21 ± 0.10)	−0.24	−1.37	1.21	NA	0.170
2.4	2.68	−0.27	−1.13...−1.38[h] (−1.26 ± 0.13)	−0.27	−1.44	1.24	NA	0.275
2.3	2.73	−0.28	−1.13...−1.48[h] (−1.30 ± 0.18)	−0.28	−1.54	1.19	NA	0.345
2.0	2.88	−0.33	−1.13...−1.59[h] (−1.36 ± 0.23)	−0.33	−1.65	1.23	NA	0.575

[a] All potentials were measured at pH 9.2 with 0.10 M Na_2SO_3 as the electron donor and are reported *vs* NHE. [b] E_{ph} is designated as the onset of the photocurrent in the photoelectrochemical scans in Figure 3A,B. [c] $E_{F,n}$ is determined from the photo-onset of the anodic photocurrent for dots above 2.6 nm in Figure 3A. [d] $E_{F,h}$ is determined from the photo-onset of the cathodic photocurrent for dots below 2.6 nm in Figure 3B. [e] E_{CB} is assigned from the peak potential of the lattice Cd^{2+} reduction feature II in Figure 4 and Figure S3. [f] E_{VB} is calculated using $E_g - E_{CB}$. [g] $E(Cd^{2+}/Cd)_{surface}$ measured from the surface Cd^{2+} reduction potential (feature I in Figure 4 and Figure S3). [h] $E_{F,n}$ range estimated from $E_{F,n}$ of 2.8 nm QD to 0.059 V below measured E_{CB} values. [i] Unit: moles H_2/[h × moles CdSe × overlap integral area].

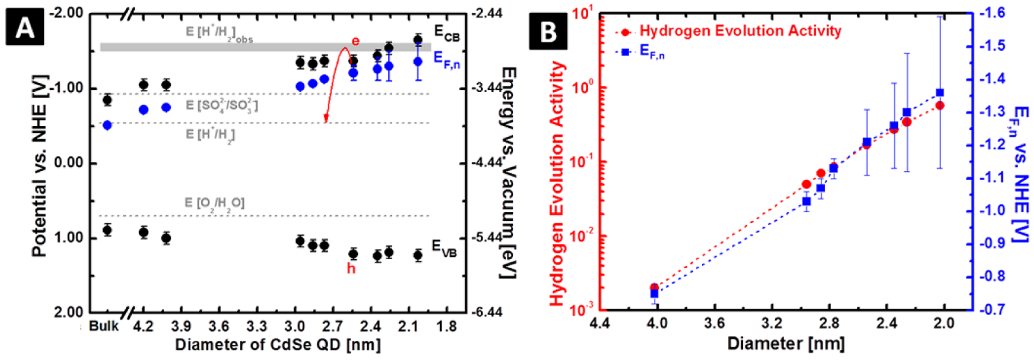

Figure 5. (A) Energy diagram for CdSe QD series, including bulk CdSe using the data from Table 1. Nernst potentials $E[H^+/H_2]$, $E[O_2/H_2O]$, and $E[SO_4^{2-}/SO_3^{2-}]$ (gray dotted lines) are calculated for the experimental condition of pH 9.2. Values for $E[H^+/H_2]_{obs}$ (the gray zone) are determined from electrochemistry in Figures 4 and S3. The separation between $E[H^+/H_2]$ and $E[H^+/H_2]_{obs}$ is due to the proton reduction overpotential over CdSe QDs. (B) Correlation between $E_{F,n}$ and photocatalytic hydrogen evolution rate for CdSe QDs.

10^{-8} and 10^{-10} A/cm^2 (Table S1). These values are very small and agree well with the low exchange current density found for metal electrodes with large hydrogen overpotentials, 10^{-10} to 10^{-12} A/cm^2 for Cd, 10^{-10} A/cm^2 for Zn, and 10^{-12} A/cm^2 for Hg.[73,74] This supports the previous hypothesis that electrochemical proton reduction occurs on the Cd^0 sites present in CdSe QDs.

The energetics data for all CdSe QDs are summarized in Table 1 and in Figure 5A. Several features are notable. As predicted by quantum size effect,[1,51] E_{CB} becomes more reducing and E_{VB} more oxidizing with diminishing QD size. However, the observed shift in E_{CB} from −0.85 to −1.65 V is much more prominent than the shift in E_{VB} from +0.89 to +1.23 V. This difference is due to the effect of different effective masses of electrons m_e* and holes m_h*. As shown in eq 2, the quantum-confined energy $E_{e/h}$ for electrons and holes is a direct function of their effective mass.[1,51]

$$E_{e/h} = \frac{\hbar^2 \pi^2}{2m^*_{e/h} a^2} \quad (2)$$

Here, a is the particle diameter, and all other variables have their common meanings. Given that m_e*(CdSe) = 0.13 m_e and m_h*(CdSe) = 0.45 m_e,[75,76] a stronger dependence of E_{CB} on the size of the QDs than that of E_{VB} is expected. This can be verified by more rigid computations.[77,78] For example, directly plotting the conduction band edge as a function of size gives a trendline of $E_{CB} \propto R^{-0.61}$ with a fitted exponent of -0.61 ± 0.04 (see Figure S5). This agrees well with the conduction band shift measured by X-ray absorption spectroscopy (yields an exponent of -0.6 ± 0.1)[79] and computed by tight-binding approximation or charge-patching method (yields exponents of −1.0 or −0.8, respectively).[80,81] Moreover, as can be seen in Figure 5A, the quasi-Fermi level of electrons $E_{F,n}$ is in general 250−300 mV below the conduction band edge E_{CB} and shifts along with E_{CB} as size decreases.

In Figure 5B, photocatalytic hydrogen evolution rates are plotted in the logarithmic form together with quasi-Fermi energies *versus* QD diameters. The correlation between the logarithmic rates and the $E_{F,n}$ values is evident. Both increase as the size of the dots decreases.

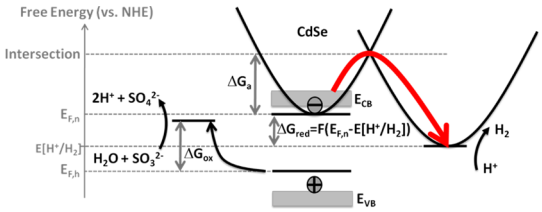

Figure 6. Schematic diagram for proton reduction at CdSe QDs. The Gibbs free energy change ΔG_{red} for electron transfer is determined by the quasi-Fermi level of electrons under illumination $E_{F,n}$ and the Nernst potential $E[H^+/H_2]$. The kinetic activation energy ΔG_a expresses the energy needed for restructuring the donor and acceptor configurations, as well as that for modifying their solvation shells and for breaking and making bonds involving H and H^+.

In the following, we show that this correlation can be understood in terms of a free-energy-controlled interfacial charge transfer. We assume that, under the photocatalytic conditions (small reaction rate and rapid stirring), mass transport of the reactants to the surface of the catalyst is not rate-limiting. Instead, the reaction rate is controlled by the solid−liquid interfacial kinetics.[82] As sketched in Figure 6, there are two half-reactions at the interface: the oxidation of sulfite and the reduction of protons. The driving force for the oxidation reaction ΔG_{ox} is given by the difference between $E_{F,h}$ and $E[SO_4^{2-}/SO_3^{2-}]$ and the driving force for the reduction reaction ΔG_{red} by the difference between $E_{F,n}$ and $E[H^+/H_2]$. Compared to ΔG_{red}, ΔG_{ox} for sulfite oxidation is large and relatively constant across the series of QDs. On the other hand, ΔG_{red} is small and strongly affected by the QD size variation as seen in Figure 5A. Thus, the proton reduction kinetics are considered to be the rate-limiting factor for the photocatalytic hydrogen evolution over CdSe QDs at pH 9.2.

The Tafel plots in Figure S4 establish cadmium metal as the site for proton reduction. Therefore, the cathodic

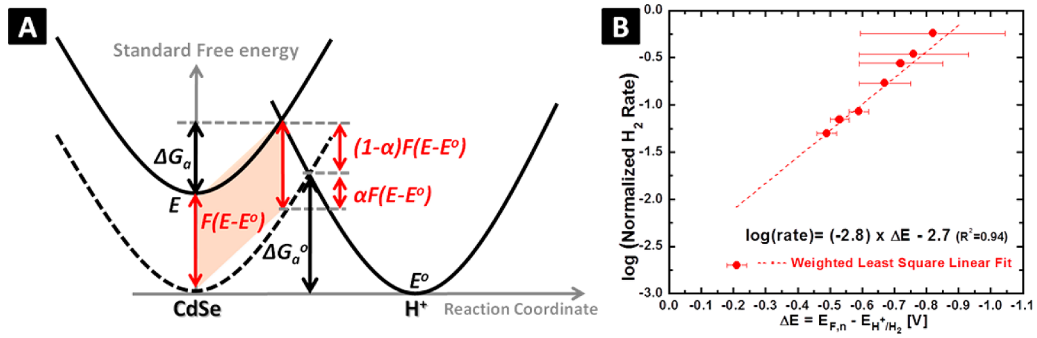

Figure 7. (A) Butler−Volmer diagram. As the QD size diminishes, the Fermi energy of electrons shifts up from E° to E, causing an increase of $F(E - E^\circ)$ in the free energy change ΔG as well as a decrease of $\alpha F(E - E^\circ)$ in the kinetic activation energy ΔG_a. The value of the electron transfer coefficient α depends on the shape of the energy surface of the reactants and the products. (B) Weighted least square linear fit of the experimental data (from Table 1 and Figure 2B). Error bars for the four smallest dots are estimated to reach from $E_{F,n}$ for the 2.8 nm QD to 0.059 V below the measured E_{CB} values and are taken into the weighted least square linear fit. The lowest point is excluded from the fit (dashed line) because the rate is close to the experimental error ($\pm 10^{-3}$) of the H_2 rate measurement.

current density can be described by the Butler−Volmer equation for electrode kinetics[82,83] as shown below:

$$j = Fk_0[H^+]e^{-\alpha F(E - E^\circ)/RT} - Fk_0[H_2]e^{(1-\alpha)F(E - E^\circ)/RT} \quad (3)$$

Here, $[H^+]$ is the concentration of the electron acceptor in the liquid (same for all QDs solutions as determined by pH) and $[H_2]$ the concentration of the electron donor; k_0 is the standard rate constant, and $F(E - E^\circ)$ is the driving force for the reaction, with F as the Faraday constant, E as the Fermi energy of electrons in the QDs $E_{F,n}$, and E° equivalent to the Nernst potential for the redox couple $E[H^+/H_2]$ in this case; α is the charge transfer coefficient as explained in Figure 7A, which determines the fraction of the increase in thermodynamic free energy change $\Delta G_{red} - \Delta G_{red}^\circ = F(E - E^\circ)$ that gets carried onto the reduction in kinetic activation energy for the forward reaction, as given by $\Delta G_a - \Delta G_a^\circ = -\alpha F(E - E^\circ)$. Importantly, the second term for the back reaction (hydrogen oxidation) in eq 3 can be ignored because the hydrogen concentration $[H_2]$ is small compared to the proton concentration $[H^+]$ even at a mild basic pH of 9.2. Converting current density to hydrogen evolution rate by taking into consideration the stoichiometry (two electrons are required to make one H_2 molecule), one obtains eq 4 and its logarithmic form, eq 5, to relate the hydrogen evolution rate to the free energy change $\Delta G_{red} = F(E_{F,n} - E[H^+/H_2]) = F\Delta E$.

$$V_{H_2} = V_{net} \approx V_{forward} = \frac{j}{2eN_A} = \frac{1}{2}k_0[H^+]e^{-\alpha F(E - E^\circ)/RT} \quad (4)$$

$$\log(V_{H_2}) = -\frac{\alpha F(E_{F,n} - E_{[H^+/H_2]})}{RT} + \log\left(\frac{1}{2}k_0[H^+]\right) = -\frac{\alpha F\Delta E}{RT} + \log\left(\frac{1}{2}k_0[H^+]\right) \quad (5)$$

A plot of eq 5 with experimental H_2 evolution rate $\log(V_{H_2})$ *versus* $\Delta E = E_{F,n} - E[H^+/H_2]$ is shown in Figure 7B. The model fits the experimental H_2 rate data well, except for the data point with the lowest rate. Here, the experimental error is large and the back reaction (hydrogen oxidation) can no longer be ignored. The fitted slope $-\alpha F/2.303RT$ is -2.8, giving an electron transfer coefficient $\alpha = 0.17-0.19$, depending on whether one uses the temperature from the electrochemical measurements (25 °C) or from the homogeneous irradiation experiments (65 °C). Literature values for α range between 0.15 and 0.5, depending on the electrode material.[84−86] Note that values for α from Figure 7B are similar to $\alpha = 0.21-0.25$ from the Tafel plots in Figure S4. The match is remarkable considering the different processes involved in the photocatalytic experiments (photogenerated electrons diffuse to the QD surface to reduce protons, whereas the photogenerated holes get captured by SO_3^{2-}) and in the dark electrochemical experiments (electrode injects electrons through QD films and reduces protons at the film−liquid interface). This further confirms that the interfacial proton reduction kinetics are the limiting factor in the photocatalytic hydrogen evolution reaction at CdSe QDs.

CONCLUSIONS

In summary, we provide the first quantitative analysis on the size dependence of photocatalytic hydrogen evolution at the solid−liquid interface. The observed behavior is analogous to size-controlled charge transfer across solid−solid interfaces, as reported by Kamat's group.[27−29] The effect can be understood by relating the electrochemical electron potential in the photoexcited dots to the activation energy for proton reduction using a modified Butler−Volmer equation. This confirms that the reactivity of the dots is controlled by their free energy. Furthermore, this work shows that the observed photocurrent inversion from anodic to cathodic in the small dots can

be understood in terms of electron trapping at the surface sites, and that proton reduction occurs on Cd(0) surface sites, as confirmed by the Tafel behavior of the proton reduction current. These results are relevant to the understanding of charge transfer at nanostructured photoelectrodes and to the engineering of advanced devices for solar energy conversion.

METHODS

Chemicals. Cadmium perchlorate (95%, Alfa Aesar), selenium powder (99.5%, Acros Organics), sodium borohydride (98%, Strem Chemicals), 2-mercaptoethanol (98%, Aldrich), sodium sulfite (98%, Merck), and potassium chloride (99.6%, Fisher Scientific) were used as received. Water was purified to a resistivity of >18 MΩ by a Nanopure II system.

Aqueous Synthesis of CdSe QDs. An aqueous synthesis developed by Rogach *et al.*[48] was adopted in this study for the preparation of CdSe QDs with 2-mercaptoethanol as the surface capping agent. After obtaining the crude product, a size refinement was performed using size-selective precipitation with 2-propanol as the nonsolvent. The size and the monodispersity of the QDs were confirmed by transmission electron microscopy (TEM), X-ray diffraction (XRD), as well as the optical band gap of the QDs using a correlation published by Schooss *et al.*[48,87]

Physical Property Characterizations. Powder XRD spectra of CdSe QDs were obtained on a Scintag XDS-2000 diffractometer with a wavelength of 0.154 nm (Cu Kα line), a tube slit divergence of 2.0 mm, a column scatter of 0.5 mm, and a receiving width of 0.2 mm. TEM samples were prepared by dipping carbon-coated copper grids into aqueous dispersions of CdSe QDs, followed by rinsing with water and air-drying. Bright-field high-resolution transmission electron microscopy (HR-TEM) images were captured on a JEOL JEM-2500 SE microscope with an accelerating voltage of 200 kV. For optical spectroscopy measurements, colloidal solutions of 0.02 mg/mL were prepared for each size of the QDs. Absorption spectra were obtained in standard quartz cuvettes using an HR2000 CG UV−vis−NIR spectrometer equipped with an Ocean Optics DH2000 deuterium/halogen light source.

Photocatalytic Hydrogen Evolution. Irradiation tests were performed by dispersing 50 mg of the QDs in 100 mL of aqueous 0.10 M Na_2SO_3 solution (as the sacrificial electron donor) in a borosilicate glass flask, followed by purging with argon and irradiating the solution mixture with a 300 W xenon arc lamp (400 mW/cm^2 at the flask surface as measured by an International Light IL1400BL photometer equipped with a GaAsP detector for 280−660 nm sensitivity range). The UV portion of the light (<330 nm) was removed by the borosilicate glass to avoid UV decomposition of the sacrificial electron donor. Evolved hydrogen was monitored as a function of time (Figure S2A) by a gas chromatograph equipped with a 60/80 Å molecular sieve column and thermal conductivity detector. The mass of the catalyst was verified gravimetrically after each irradiation using selective precipitation with hydrochloric acid. Hydrogen evolution rates were obtained from the hydrogen−time data, after correcting first for catalyst mass (Figure S2B) and then with regard to absorbed photons. The latter correction was performed by dividing the mass-normalized rates with the overlap integral of the absorbance spectrum of the respective QD and the emission spectrum of the Xe lamp (Figure S2C), as detailed elsewhere.[41]

Photoelectrochemical Measurements. CdSe QD-coated film (1.0 × 1.0 cm^2) electrodes were prepared on F/SnO_2 substrates (MTI Corporation, resistivity = 12−14 ohm/sq) by drop-coating QD solutions and drying in dark overnight at room temperature. F/SnO_2 substrates were precleaned by consecutive sonications in acetone, methanol, and isopropyl alcohol. After the QD films were dried, silver wire was attached to the F/SnO_2 substrate with carbon tape and sealed with polymer adhesive. Electrochemistry and photoelectrochemistry measurements were performed using a three-electrode cell with a quartz front window, a KCl-bridged saturated calomel electrode (SCE) as the reference electrode, a Pt coil as the counter electrode, and the CdSe QD film on F/SnO_2 as the working electrode. A 50 mL volume of electrolyte made of 1.0 M KCl and 0.10 M Na_2SO_3 aqueous solution with a pH of 9.2 was added to the cell and degassed with N_2 prior to the measurements. Na_2SO_3 was used as a sacrificial electron donor to resemble the condition in the hydrogen evolution tests. Cathodic potential scans were recorded from 0.4 to −1.7 V both in the dark and under chopped (front side) illumination with a scan rate of 10 mV/s using a Gamry Reference 600 potentiostat. Illumination was provided by a 300 W Xe arc lamp connected to the cell through a SiO_2 fiber-optic cable (120 ± 20 mW/cm^2 at the electrode as measured by an International Light IL1400BL photometer equipped with a GaAsP detector for 280−660 nm range). The potential measurements were calibrated using the standard potential of $K_3[Fe(CN)_6]$ (+0.358 V *vs* NHE).

Conflict of Interest: The authors declare no competing financial interest.

Acknowledgment. We are grateful for financial support from Research Corporation for Science Advancement (Scialog award) and from the National Science Foundation (NSF, Grants 0829142 and 1133099).

Supporting Information Available: Results including XRD spectra of CdSe QDs, correction details for H_2 evolution rate, additional dark electrochemical scans, Tafel plots, and fitting results for proton reduction over CdSe QD films and E_{CB} *versus* QD diameter trend plot. This material is available free of charge *via* the Internet at http://pubs.acs.org.

REFERENCES AND NOTES

1. Brus, L. E. A Simple Model for the Ionization Potential, Electron Affinity, and Aqueous Redox Potentials of Small Semiconductor Crystallites. *J. Chem. Phys.* **1983**, *79*, 5566–5571.
2. Dingle, R.; Wiegmann, W.; Henry, C. Quantum States of Confined Carriers in Very Thin $Al_xGa_{1-x}As$-GaAs-Al_xGa_{1-x}As Heterostructures. *Phys. Rev. Lett.* **1974**, *33*, 827–830.
3. Henglein, A. Photo-Degradation and Fluorescence of Colloidal-Cadmium Sulfide in Aqueous Solution. *Ber. Bunsen-Ges. Phys. Chem.* **1982**, *86*, 301–305.
4. Fojtik, A.; Weller, H.; Koch, U.; Henglein, A. Photo-Chemistry of Colloidal Metal Sulfides. 8. Photo-Physics of Extremely Small CdS Particles: Q-State CdS and Magic Agglomeration Numbers. *Ber. Bunsen-Ges. Phys. Chem.* **1984**, *88*, 969–977.
5. Kayanuma, Y. Quantum-Size Effects of Interacting Electrons and Holes in Semiconductor Microcrystals with Spherical Shape. *Phys. Rev. B* **1988**, *38*, 9797–9805.
6. Sim, H.-S.; Ahn, K.-H.; Chang, K.; Ihm, G.; Kim, N.; Lee, S. Magnetic Edge States in a Magnetic Quantum Dot. *Phys. Rev. Lett.* **1998**, *80*, 1501–1504.
7. Sim, H.-S.; Ihm, G.; Kim, N.; Chang, K. Magnetic Quantum Dot: A Magnetic Transmission Barrier and Resonator. *Phys. Rev. Lett.* **2001**, *87*, 146601.
8. Valden, M. Onset of Catalytic Activity of Gold Clusters on Titania with the Appearance of Nonmetallic Properties. *Science* **1998**, *281*, 1647–1650.
9. Wilker, M. B.; Schnitzenbaumer, K. J.; Dukovic, G. Recent Progress in Photocatalysis Mediated by Colloidal II−VI Nanocrystals. *Isr. J. Chem.* **2012**, *52*, 1002–1015.
10. Grätzel, M. Photoelectrochemical Cells. *Nature* **2001**, *414*, 338–344.

11. Lewis, N. S.; Crabtree, G. W. In *Basic Research Needs for Solar Energy Utilization*; Lewis, N. S., Crabtree, G. W., Eds.; Department of Energy, 2005.
12. Lewis, N. S.; Nocera, D. G. Powering the Planet: Chemical Challenges in Solar Energy Utilization. *Proc. Natl. Acad. Sci. U.S.A.* **2006**, *103*, 15729–15735.
13. Osterloh, F. E. Inorganic Materials as Catalysts for Photochemical Splitting of Water. *Chem. Mater.* **2008**, *20*, 35–54.
14. Kudo, A.; Miseki, Y. Heterogeneous Photocatalyst Materials for Water Splitting. *Chem. Soc. Rev.* **2009**, *38*, 253–278.
15. Maeda, K.; Domen, K. Photocatalytic Water Splitting: Recent Progress and Future Challenges. *J. Phys. Chem. Lett.* **2010**, *1*, 2655–2661.
16. Osterloh, F. E.; Parkinson, B. A. Recent Developments in Solar Water-Splitting Photocatalysis. *MRS Bull.* **2011**, *36*, 17–22.
17. Osterloh, F. E. Inorganic Nanostructures for Photoelectrochemical and Photocatalytic Water Splitting. *Chem. Soc. Rev.* **2013**, *42*, 2294–2320.
18. Duret, A.; Grätzel, M. Visible Light-Induced Water Oxidation on Mesoscopic α-Fe_2O_3 Films Made by Ultrasonic Spray Pyrolysis. *J. Phys. Chem. B* **2005**, *109*, 17184–17191.
19. Cesar, I.; Kay, A.; Gonzalez Martinez, J. A.; Grätzel, M. Translucent Thin Film Fe_2O_3 Photoanodes for Efficient Water Splitting by Sunlight: Nanostructure-Directing Effect of Si-Doping. *J. Am. Chem. Soc.* **2006**, *128*, 4582–4583.
20. Klahr, B. M.; Hamann, T. W. Current and Voltage Limiting Processes in Thin Film Hematite Electrodes. *J. Phys. Chem. C* **2011**, *115*, 8393–8399.
21. Townsend, T. K.; Sabio, E. M.; Browning, N. D.; Osterloh, F. E. Photocatalytic Water Oxidation with Suspended alpha-Fe_2O_3 Particles—Effects of Nanoscaling. *Energy Environ. Sci.* **2011**, *4*, 4270–4275.
22. Frame, F. A.; Townsend, T. K.; Chamousis, R. L.; Sabio, E. M.; Dittrich, T.; Browning, N. D.; Osterloh, F. E. Photocatalytic Water Oxidation with Nonsensitized IrO_2 Nanocrystals under Visible and UV Light. *J. Am. Chem. Soc.* **2011**, *133*, 7264–7267.
23. Gerischer, H. The Impact of Semiconductors on the Concepts of Electrochemistry. *Electrochim. Acta* **1990**, *35*, 1677–1699.
24. Marcus, R. Chemical and Electrochemical Electron-Transfer Theory. *Annu. Rev. Phys. Chem.* **1964**, *15*, 155–196.
25. Chuang, C.-H.; Doane, T. L.; Lo, S. S.; Scholes, G. D.; Burda, C. Measuring Electron and Hole Transfer in Core/Shell Nanoheterostructures. *ACS Nano* **2011**, *5*, 6016–6124.
26. Scholes, G. D.; Jones, M.; Kumar, S. Energetics of Photoinduced Electron-Transfer Reactions Decided by Quantum Confinement. *J. Phys. Chem. C* **2007**, *111*, 13777–13785.
27. Tvrdy, K.; Kamat, P. V. Photoinduced Electron Transfer from Semiconductor Quantum Dots to Metal Oxide Nanoparticles. *Proc. Natl. Acad. Sci. U.S.A.* **2011**, *108*, 29–34.
28. Kongkanand, A.; Tvrdy, K.; Takechi, K.; Kuno, M.; Kamat, P. V. Quantum Dot Solar Cells. Tuning Photoresponse through Size and Shape Control of CdSe-TiO_2 Architecture. *J. Am. Chem. Soc.* **2008**, *130*, 4007–4015.
29. Robel, I.; Kuno, M.; Kamat, P. V. Size-Dependent Electron Injection from Excited CdSe Quantum Dots into TiO_2 Nanoparticles. *J. Am. Chem. Soc.* **2007**, *129*, 4136–4137.
30. Robel, I.; Subramanian, V.; Kuno, M.; Kamat, P. V. Quantum Dot Solar Cells. Harvesting Light Energy with CdSe Nanocrystals Molecularly Linked to Mesoscopic TiO_2 Films. *J. Am. Chem. Soc.* **2006**, *128*, 2385–2393.
31. Bang, J. H.; Kamat, P. V. CdSe Quantum Dot−Fullerene Hybrid Nanocomposite for Solar Energy Conversion: Electron Transfer and Photoelectrochemistry. *ACS Nano* **2011**, *5*, 9421–9427.
32. Kamat, P. V. Manipulation of Charge Transfer Across Semiconductor Interface. A Criterion That Cannot Be Ignored in Photocatalyst Design. *J. Phys. Chem. Lett.* **2012**, *3*, 663–672.
33. Scholz, F.; Dworak, L.; Matylitsky, V. V.; Wachtveitl, J. Ultrafast Electron Transfer from Photoexcited CdSe Quantum Dots to Methylviologen. *ChemPhysChem* **2011**, *12*, 2255–2259.
34. Huang, J.; Stockwell, D.; Huang, Z.; Mohler, D. L.; Lian, T. Photoinduced Ultrafast Electron Transfer from CdSe Quantum Dots to Re-Bipyridyl Complexes. *J. Am. Chem. Soc.* **2008**, *130*, 5632–5633.
35. Tanaka, D.; Oaki, Y.; Imai, H. Enhanced Photocatalytic Activity of Quantum-Confined Tungsten Trioxide Nanoparticles in Mesoporous Silica. *Chem. Commun.* **2010**, *46*, 5286–5288.
36. Waller, M. R.; Townsend, T. K.; Zhao, J.; Sabio, E. M.; Chamousis, R. L.; Browning, N. D.; Osterloh, F. E. Single-Crystal Tungsten Oxide Nanosheets: Photochemical Water Oxidation in the Quantum Confinement Regime. *Chem. Mater.* **2012**, *24*, 698–704.
37. Yanagida, S.; Ogata, T.; Shindo, A.; Hosokawa, H.; Mori, H.; Sakata, T.; Wada, Y. Semiconductor Photocatalysis: 1) Size Control of Surface-Capped CdS Nanocrystallites and the Quantum Size Effect in Their Photocatalysis. *Bull. Chem. Soc. Jpn.* **1995**, *68*, 752–758.
38. Pal, B.; Torimoto, T.; Iwasaki, K.; Shibayama, T.; Takahashi, H.; Ohtani, B. Size and Structure-Dependent Photocatalytic Activity of Jingle-Bell-Shaped Silica-Coated Cadmium Sulfide Nanoparticles for Methanol Dehydrogenation. *J. Phys. Chem. B* **2004**, *108*, 18670–18674.
39. Frame, F. A.; Carroll, E. C.; Larsen, D. S.; Sarahan, M.; Browning, N. D.; Osterloh, F. E. First Demonstration of CdSe as a Photocatalyst for Hydrogen Evolution from Water under UV and Visible Light. *Chem. Commun.* **2008**, 2206–2208.
40. Frame, F. A.; Osterloh, F. E. CdSe-MoS_2: A Quantum Size-Confined Photocatalyst for Hydrogen Evolution from Water under Visible Light. *J. Phys. Chem. C* **2010**, *114*, 10628–10633.
41. Holmes, M. A.; Townsend, T. K.; Osterloh, F. E. Quantum Confinement Controlled Photocatalytic Water Splitting by Suspended CdSe Nanocrystals. *Chem. Commun.* **2012**, *48*, 371–373.
42. Hodes, G. Nanocrystalline Photoelectrochemical Cells. *J. Electrochem. Soc.* **1992**, *139*, 3136–3140.
43. Cesar, I.; Sivula, K.; Kay, A.; Zboril, R.; Gratzel, M. Influence of Feature Size, Film Thickness, and Silicon Doping on the Performance of Nanostructured Hematite Photoanodes for Solar Water Splitting. *J. Phys. Chem. C* **2009**, *113*, 772–782.
44. Hagfeldt, A.; Gratzel, M. Light-Induced Redox Reactions in Nanocrystalline Systems. *Chem. Rev.* **1995**, *95*, 49–68.
45. Memming, R. Photoinduced Charge Transfer Processes at Semiconductor Electrodes and Particles. *Top. Curr. Chem.* **1994**, *169*, 105–181.
46. Sambur, J. B.; Novet, T.; Parkinson, B. A. Multiple Exciton Collection in a Sensitized Photovoltaic System. *Science* **2010**, *330*, 63–66.
47. Han, Z.; Qiu, F.; Eisenberg, R.; Holland, P. L.; Krauss, T. D. Robust Photogeneration of H_2 in Water Using Semiconductor Nanocrystals and a Nickel Catalyst. *Science* **2012**, *338*, 1321–1324.
48. Rogach, A. L.; Kornowski, A.; Gao, M.; Eychmüller, A.; Weller, H. Synthesis and Characterization of a Size Series of Extremely Small Thiol-Stabilized CdSe Nanocrystals. *J. Phys. Chem. B* **1999**, *103*, 3065–3069.
49. Vossmeyer, T.; Katsikas, L.; Giersig, M.; Popovic, I. G.; Diesner, K.; Chemseddine, A.; Eychmuller, A.; Weller, H. CdS Nanoclusters: Synthesis, Characterization, Size Dependent Oscillator Strength, Temperature Shift of the Excitonic Transition Energy, and Reversible Absorbance Shift. *J. Phys. Chem.* **1994**, *98*, 7665–7673.
50. Rogach, A. L.; Katsikas, L.; Kornowski, A.; Su, D.; Eychmuller, A.; Weller, H. Synthesis and Characterization of Thiol-Stabilized CdTe Nanocrystals. *Ber. Bunsen-Ges. Phys. Chem.* **1996**, *100*, 1772–1778.
51. Rossetti, R.; Ellison, J. L.; Gibson, J. M.; Brus, L. E. Size Effects in the Excited Electronic States of Small Colloidal CdS Crystallites. *J. Chem. Phys.* **1984**, *80*, 4464–4469.
52. Gerischer, H.; Lubke, M. A Particle Size Effect in the Sensitization of TiO_2 Electrodes by a CdS Deposit. *J. Electroanal. Chem.* **1986**, *204*, 225–227.

53. Soloviev, V. N.; Eichhöfer, A.; Fenske, D.; Banin, U. Size-Dependent Optical Spectroscopy of a Homologous Series of CdSe Cluster Molecules. *J. Am. Chem. Soc.* **2001**, *123*, 2354–2364.
54. Norris, D. J.; Bawendi, M. G. Measurement and Assignment of the Size-Dependent Optical Spectrum in CdSe Quantum Dots. *Phys. Rev. B* **1996**, *53*, 16338–16346.
55. Buhler, N.; Meier, K.; Reber, J. F. Photochemical Hydrogen Production with Cadmium Sulfide Suspensions. *J. Phys. Chem.* **1984**, *88*, 3261–3268.
56. Reber, J. F.; Meier, K. Photochemical Production of Hydrogen with Zinc Sulfide Suspensions. *J. Phys. Chem.* **1984**, *88*, 5903–5913.
57. Peter, L. M.; Wijayantha, K. G. U.; Riley, D. J.; Waggett, J. P. Band-Edge Tuning in Self-Assembled Layers of Bi_2S_3 Nanoparticles Used To Photosensitize Nanocrystalline TiO_2. *J. Phys. Chem. B* **2003**, *107*, 8378–8381.
58. Abeles, B.; Sheng, P.; Coutts, M. D.; Arie, Y. Structural and Electrical Properties of Granular Metal Films. *Adv. Phys.* **1975**, *24*, 407–461.
59. Terrill, R.; Postlethwaite, T. Monolayers in Three Dimensions: NMR, SAXS, Thermal, and Electron Hopping Studies of Alkanethiol Stabilized Gold Clusters. *J. Am. Chem. Soc.* **1995**, *117*, 12537–12548.
60. Sodergren, S.; Hagfeldt, A.; Olsson, J.; Lindquist, S. E. Theoretical Models for the Action Spectrum and the Current-Voltage Characteristics of Microporous Semiconductor Films in Photoelectrochemical Cells. *J. Phys. Chem.* **1994**, *98*, 5552–5556.
61. Hagfeldt, A.; Björkstén, U.; Lindquist, S. E. Photoelectrochemical Studies of Colloidal TiO_2-Films: The Charge Separation Process Studied by Means of Action Spectra in the UV Region. *Sol. Energy Mater. Sol. Cells* **1992**, *27*, 293–304.
62. Bisquert, J.; Vikhrenko, V. S. Interpretation of the Time Constants Measured by Kinetic Techniques in Nanostructured Semiconductor Electrodes and Dye-Sensitized Solar Cells. *J. Phys. Chem. B* **2004**, *108*, 2313–2322.
63. Hagfeldt, A.; Lindstrom, H.; Sodergren, S.; Lindquist, S. E. Photoelectrochemical Studies of Colloidal TiO_2 Films—The Effect of Oxygen Studied by Photocurrent Transients. *J. Electroanal. Chem.* **1995**, *381*, 39–46.
64. Kronik, L.; Ashkenasy, N.; Leibovitch, M.; Fefer, E.; Shapira, Y.; Gorer, S.; Hodes, G. Surface States and Photovoltaic Effects in CdSe Quantum Dot Films. *J. Electrochem. Soc.* **1998**, *145*, 1748–1755.
65. Hodes, G.; Howell, I. D. J.; Peter, L. M. In *Photochemical and Photoelectrochemical Conversion and Storage of Solar Energy (Proc. IPS-9)*; Tian, Z. W., Cao, Y., Eds.; Internaional Academic Publishers: Beijing, 1993; p 331.
66. Hodes, G.; Albu-Yaron, A. The Electrochemical Society Proceedings Series. In *Photoelectrochemistry and Electrosynthesis on Semiconducting Materials (The Electrochemical Society Proceedings Series, PV 88-14)*; Ginley, D. S., Honda, K., Nozik, A., Fujishima, A., Armstrong, N., Sakata, T., Kawai, T., Eds.; Electrochemical Society: Pennington, NJ, 1988; p 298.
67. Frese, K. W. Electrochemical Studies of Photocorrosion of n-CdSe. *J. Electrochem. Soc.* **1983**, *130*, 28–33.
68. Tan, M. X.; Laibinis, P. E.; Nguyen, S. T.; Kesselman, J. M.; Stanton, C. E.; Lewis, N. S. Principles and Applications of Semiconductor Photoelectrochemistry. *Prog. Inorg. Chem.* **1994**, *41*, 21–144.
69. Albery, W. J. The Transport and Kinetics of Photogenerated Carriers in Colloidal Semiconductor Electrode Particles. *J. Electrochem. Soc.* **1984**, *131*, 315–325.
70. Regan, B. O.; Moser, J.; Anderson, M.; Gratzel, M. Vectorial Electron Injection into Transparent Semiconductor Membranes and Electric Field Effects on the Dynamics of Light-Induced Charge Separation. *J. Phys. Chem.* **1990**, *94*, 8720–8726.
71. Querner, C.; Reiss, P.; Sadki, S.; Zagorska, M.; Pron, A. Size and Ligand Effects on the Electrochemical and Spectroelectrochemical Responses of CdSe Nanocrystals. *Phys. Chem. Chem. Phys.* **2005**, *7*, 3204–3209.
72. Poznyak, S. K.; Osipovich, N. P.; Shavel, A.; Talapin, D. V.; Gao, M.; Eychmüller, A.; Gaponik, N. Size-Dependent Electrochemical Behavior of Thiol-Capped CdTe Nanocrystals in Aqueous Solution. *J. Phys. Chem. B* **2005**, *109*, 1094–1100.
73. Bard, A. J.; Parsons, R.; Jordan, J. *Standard Potentials in Aqueous Solution*, 1st ed.; Marcel Dekker: New York, 1985; p 43.
74. Sawyer, D. T.; Sobkowiak, A.; Roberts, J. L. *Electrochemistry for Chemists*, 2nd ed.; John Wiley & Sons: New York, 1995; p 207.
75. Gaponenki, S. V. *Optical Properties of Semiconductor Nanocrystals*; Cambridge University Press: New York, 1998; p 19.
76. Beard, M. C.; Turner, G. M.; Schmuttenmaer, C. A. Size-Dependent Photoconductivity in CdSe Nanoparticles As Measured by Time-Resolved Terahertz Spectroscopy. *Nano Lett.* **2002**, *2*, 983–987.
77. Efros, A. L.; Rosen, M. The Electronic Structure of Semiconductor Nanocrystals. *Annu. Rev. Mater. Sci.* **2000**, *30*, 475–521.
78. Efros, A.; Rosen, M. Quantum Size Level Structure of Narrow-Gap Semiconductor Nanocrystals: Effect of Band Coupling. *Phys. Rev. B* **1998**, *58*, 7120–7135.
79. Lee, J.; Meulenberg, R.; Hanif, K.; Mattoussi, H.; Klepeis, J.; Terminello, L.; Van Buuren, T. Experimental Observation of Quantum Confinement in the Conduction Band of CdSe Quantum Dots. *Phys. Rev. Lett.* **2007**, *98*, 146803.
80. Lippens, P. E.; Lannoo, M. Comparison between Calculated and Experimental Values of the Lowest Excited Electronic State of Small CdSe Crystallites. *Phys. Rev. B* **1990**, *41*, 6079–6081.
81. Wang, L.; Li, J. First-Principles Thousand-Atom Quantum Dot Calculations. *Phys. Rev. B* **2004**, *69*, 153302.
82. Bard, A. J.; Faulkner, L. R. *Electrochemical Methods: Fundamentals and Applications*; John Wiley & Sons: New York, 2001; pp 92−98.
83. Gratzel, M.; Frank, A. J. Interfacial Electron-Transfer Reactions in Colloidal Semiconductor Dispersions. Kinetic Analysis. *J. Phys. Chem.* **1982**, *86*, 2964–2967.
84. Rieger, P. H. *Electrochemistry*; Prentice-Hall: London, 1987; pp 315−350.
85. Fletcher, S. Tafel Slopes from First Principles. *J. Solid State Electrochem.* **2009**, *13*, 537–549.
86. Meng, Y.; Aldous, L.; Belding, S. R.; Compton, R. G. The Hydrogen Evolution Reaction in a Room Temperature Ionic Liquid: Mechanism and Electrocatalyst Trends. *Phys. Chem. Chem. Phys.* **2012**, *14*, 5222–5228.
87. Schooss, D.; Mews, A.; Eychmuller, A.; Weller, H. Quantum-Dot Quantum Well CdS/HgS/CdS: Theory and Experiment. *Phys. Rev. B* **1994**, *49*, 17072–17078.